AIAA 2001-0273
Secondary Görtler Instability In Hypersonic Boundary Layers

Chong W. Whang and Xiaolin Zhong
University of California, Los Angeles
Los Angeles, CA

39th Aerospace Sciences Meeting & Exhibit
January 8–11, 2001 / Reno, NV

Secondary Görtler Instability in Hypersonic Boundary Layers

Chong W. Whang *and Xiaolin Zhong †

University of California, Los Angeles, California 90095

Abstract

Secondary Görtler instability in hypersonic boundary layers is studied in this paper. The nonlinear development of Görtler vortices distorts the mean flow and leads highly inflectional profiles not only in wall normal direction but also in spanwise direction which induce the secondary instability. In the break-down process of Görtler vortices, unsteady fluctuations appear in the vortices. Such process is through a secondary instability. In this paper, secondary instability of hypersonic Görtler vortices is studied using two-dimensional linear stability analysis and numerical simulations. A two-dimensional linear stability code is developed in order to find secondary modes of hypersonic Görtler vortices. The mode obtained by linear stability analysis is imposed at the entrance of the computational domain. Subsequent development of the secondary mode is carried out by solving the full Navier-Stokes equations. We investigate secondary Görtler instabilities in hypersonic boundary layers.

1 Introduction

Longitudinal counter rotating vortices appear in boundary layer flow along the concave surface. These vortices are called Görtler vortices and affect the flow instability in boundary layers along the concave surface. Görtler vortices have been studied experimentally and numerically since Görtler first studied them in 1940 [1]. Linear and nonlinear developments, and break-down of Görtler vortices in incompressible boundary layers along the concave surfaces had been studied experimentally. [2-7] Aihara [2] showed that the nonlinear development of Görtler vortices mainly affects the transition of the boundary layers. He imposed artificial impulsive disturbances on the existence of Görtler vortices. He found that the imposed disturbances amplify or decay in the linear region of Görtler vortices depending on the initial value of the excita-

tion, but the disturbances rapidly grow in the nonlinear region. Winoto and Crane [3] measured streamwise and spanwise mean velocity components using laser anemometry in developing laminar flow in a water channel experiment. Hydrogen bubble flow was used to visualize the naturally occurring pattern of Görtler vortices. They found the unsteadiness of Görtler vortices at high Reynolds numbers. Using laser induced fluorescence technique, Peerhossaini and Wesfreid [4] observed the development of the mushroom-shaped vortices due to the nonlinear growth of Görtler vortices. By a laser anemometry measurement of velocity field, they found two regions in the development of Görtler vortices. The first region is the up-wash in which flow particles move outward from the wall. The second region is the down-wash in which the particles are forced toward the wall. Görtler vortices are spatially evolving steady disturbances, but due to the secondary instability effects, unsteady oscillations appear in the vortices. Peerhossaini and Wesfreid found that such oscillations first appear in the up-wash region. They also observed the interaction between two neighboring vortices in the spanwise direction. Such interaction leads to attraction and swallowing of the vortices as the Görtler number increases.

Recent experiments have shown that the breakdown of Görtler vortices is mainly due to the secondary instabilities which are nonlinear interactions between the Görtler mode and the shear mode in the boundary layers. Aihara and Kohama [5] and Aihara et al [6] showed that the breakdown of the Görtler vortex structure into a horseshoe-vortex structure because of the secondary instability. Swearingen and Blackwelder [7] identified the two kinds of secondary instabilities to be the sinuous and varicose (horseshoe) types. They showed that the sinuous mode is produced by spanwise velocity gradient, and the varicose is due to normal velocity gradient. In their experiments, the unsteady secondary instability fluctuations were mainly the sinuous mode. They concluded that the sinuous mode plays a more important role in transition to turbulence of Görtler vortices.

Nonlinear developments and secondary instability of Görtler vortices had been investigated using the direct numerical simulations especially for incompress-

---

*Graduate Student, chong@seas.ucla.edu

†Associate Professor, Mechanical and Aerospace Engineering Department, Associate Fellow AIAA

ible flow. [8-14] The results showed that the nonlinear effects of Görtler vortices produce inflection points in the spanwise direction as well as the wall normal direction which induce the secondary instabilities. Hall [8] numerically integrated the nonlinear partial differential equations for finite wave number of the vortices and demonstrated that nonlinear evolution of streamwise Görtler vortices produces inflectional profiles which will presumably break down. Denier and Hall [9] investigated the spatial nonlinear evolution of the fastest growing Görtler vortex and found that the nonlinear development of the Görtler mode results in a reversed flow. However, inflection profiles develop earlier than such separation flow, so they concluded that it has a little effect on transition. Sabry and Liu [10] simulated the nonlinear development of Görlter vortices by solving a time dependent, quasi-two-dimensional formulation which simplified the computational framework. A spatial development of Görtler vortices was related to temporal calculations by a constant convection velocity. They compared their numerical results with previous experimental works of Swearingen and Blackwelder [7] and Ito [15]. The quantitative comparison with the structural aspects of the experiments showed good agreements. Lee and Liu [11] simulated spatially growing longitudinal vortices by a finite difference algorithm in solving the three-dimensional parabolized Navier-Stokes equations. Their results compared well with those from Swearingen and Blackwelder [7].

Liu and Domaradzki [12], Yu and Liu [13], and Li and Malik [14] studied secondary instability effects on Görtler vortices. Liu and Domaradzki [12] solved the full three-dimensional Navier-Stokes equations to investigate transition to turbulence of Görtler vortices. Their flow conditions were the same as those by Swearingen and Blackwelder [7]. Initial disturbances were obtained from LST. They showed that Görtler vortices become turbulent due to the spanwise velocity gradient as well as the normal velocity gradient. These velocity profiles contain inflection points which affect the flow instabilities in boundary layers. They showed that the varicose mode is related to the normal velocity gradient, and the sinuous mode is to the spanwise gradient and concluded that the sinuous mode dominates the varicose. Li and Malik [14] used two-dimensional LST and three-dimensional PSE (parabolic stability equation) methods and studied nonlinear secondary instability effects on Görtler vortices. In their approaches, they showed there are two kinds of the secondary instability modes; even and odd. The even mode is related to the varicose mode, and the odd mode is to the sinuous mode. Their linear stability analysis showed that for the large wave length of Görtler vortices, the even modes are dominant, and for the short wave length, the odd modes have main roles for

transition. They explained that it is the reason why some experiments [5] [6] showed a varicose mode dominant break-down, but other experiment [7] showed a sinuous mode.

Secondary Görtler instability in incompressible boundary layers had been studied extensively, but hypersonic Görtler instability is not well understood. In this paper, we study secondary instability of hypersonic Görtler vortices using two-dimensional linear stability analysis and numerical simulations.

2   Formulation

Governing equations and numerical methods for 2-D linear stability theory and direct numerical simulation are discussed. The full linearized compressible Navier-Stokes equations in cartesian coordinate system are derived. Wall curvature effects are included in LST analysis using a coordinate transformation. In the numerical simulation, the full Navier-Stokes equations are solved using a fifth order explicit upwind shock fitting scheme. Governing equations and numerical methods for the linear stability analysis and numerical simulation are explained as follow.

2.1   2-D Linear Stability Analysis

The compressible linear stability equations originate from the compressible Navier-Stokes equations. The gas is assumed to be perfect Newtonian gas. The three-dimensional Navier-Stokes equations in cartesian coordinates (x^*, y^*, z^*) are

$$\rho^* \left[\frac{\partial \mathbf{u}^*}{\partial t^*} + \mathbf{u}^* \cdot \nabla \mathbf{u}^* \right] = -\nabla p^* + \nabla \cdot [\lambda^* (\nabla \cdot \mathbf{u}^*) \mathbf{I} + \mu^* (\nabla \mathbf{u}^* + \nabla \mathbf{u}^{*tr})], \quad (1)$$

$$\frac{\partial \rho^*}{\partial t^*} + \nabla \cdot (\rho^* \mathbf{u}^*) = 0, \quad (2)$$

$$\rho^* c_p^* \left[\frac{\partial T^*}{\partial t^*} + \mathbf{u}^* \cdot \nabla T^* \right] = \nabla \cdot (k^* \nabla T^*) + \frac{\partial p^*}{\partial t^*} + \mathbf{u}^* \cdot \nabla p^* + \Phi^*, \quad (3)$$

$$p^* = \rho^* R^* T^*, \quad (4)$$

where '*' denotes dimensional quantities. $\mathbf{u}^*$ is the velocity vector, ρ^* is the density, p^* is the pressure, T^* is the temperature, R^* is the gas constant, c_p^* is the

specific heat at constant pressure, k^* is the thermal conductivity, μ^* is the first coefficient of viscosity, and λ^* is the second coefficient of viscosity. The viscosity coefficient is determined by Sutherland's law. The viscous dissipation function, Φ^*, is given as

$$\Phi^* = \lambda^*(\nabla \cdot \mathbf{u}^*)^2 + \frac{\mu^*}{2}[\nabla \mathbf{u}^* + \nabla \mathbf{u}^{*tr}]^2 . \tag{5}$$

The flow variables and equations are nondimensionalized as follows: velocity by U_∞^*, density by ρ_∞^*, pressure by $\rho_\infty^* U_\infty^{*2}$, length scales by x^*, and time scale by x^*/U_∞^* where x^* denotes a distance from the leading edge. Instantaneous flow variables are represented as the sum of mean value and fluctuation, i.e.

$$q = \bar{q}(x, y, z) + \tilde{q}(x, y, z, t) \tag{6}$$

Resulting linear disturbance equations can be expressed in matrix form as

$$\begin{aligned} &[A]\tilde{\mathbf{q}} + [B]\tfrac{\partial \tilde{\mathbf{q}}}{\partial t} + [C]\tfrac{\partial \tilde{\mathbf{q}}}{\partial x} + [D]\tfrac{\partial \tilde{\mathbf{q}}}{\partial y} \\ &+[E]\tfrac{\partial \tilde{\mathbf{q}}}{\partial z} + [F]\tfrac{\partial^2 \tilde{\mathbf{q}}}{\partial x^2} + [G]\tfrac{\partial^2 \tilde{\mathbf{q}}}{\partial y^2} + [H]\tfrac{\partial^2 \tilde{\mathbf{q}}}{\partial z^2} \\ &+[I]\tfrac{\partial^2 \tilde{\mathbf{q}}}{\partial x \partial y} + [J]\tfrac{\partial^2 \tilde{\mathbf{q}}}{\partial y \partial z} + [L]\tfrac{\partial^2 \tilde{\mathbf{q}}}{\partial x \partial z} = 0 , \end{aligned} \tag{7}$$

where $\tilde{\mathbf{q}} = \{\tilde{u}, \tilde{v}, \tilde{p}, \tilde{T}, \tilde{w}\}^{tr}$. All matrix coefficients are function of mean values. A coordinate transformations is applied to equation (7) to transform cartesian coordinate (x,y,z) into curve linear system (ξ, η, ζ). Transformation gives new matrix form of the disturbance equations:

$$\begin{aligned} &[A']\tilde{\mathbf{q}}_1 + [B']\tfrac{\partial \tilde{\mathbf{q}}_1}{\partial \tau} + [C']\tfrac{\partial \tilde{\mathbf{q}}_1}{\partial \xi'} + [D']\tfrac{\partial \tilde{\mathbf{q}}_1}{\partial \eta'} \\ &+[E']\tfrac{\partial \tilde{\mathbf{q}}_1}{\partial \zeta'} + [F']\tfrac{\partial^2 \tilde{\mathbf{q}}_1}{\partial \xi'^2} + [G']\tfrac{\partial^2 \tilde{\mathbf{q}}_1}{\partial \eta'^2} + [H']\tfrac{\partial^2 \tilde{\mathbf{q}}_1}{\partial \zeta'^2} \\ &+[I']\tfrac{\partial^2 \tilde{\mathbf{q}}_1}{\partial \xi' \partial \eta'} + [J']\tfrac{\partial^2 \tilde{\mathbf{q}}_1}{\partial \eta' \partial \zeta'} + [L']\tfrac{\partial^2 \tilde{\mathbf{q}}_1}{\partial \xi' \partial \zeta'} = 0 , \end{aligned} \tag{8}$$

where $\tilde{\mathbf{q}}_1 = \{\tilde{u}', \tilde{v}', \tilde{p}', \tilde{T}', \tilde{w}'\}^{tr}$.

Secondary disturbance form is

$$\tilde{\mathbf{q}} = \hat{\mathbf{q}}(\eta, \zeta)e^{\alpha \xi - \omega \tau} , \tag{9}$$

Equation (8) and (9) constitute an eigenvalue problem which is solved by using a fourth order finite difference in the wall normal direction and a Fourier collocation method in the spanwise direction. The discretized system can be represented in the form

$$\mathbf{A}\hat{\mathbf{q}} = \alpha \hat{\mathbf{q}} , \tag{10}$$

Since the basic flow state is symmetric, the eigenfunctions can be split into families of even (varicose) and odd (sinuous) modes. For varicose modes, all eigenfunctions except spanwise velocity are symmetric, but those for sinuous modes are anti-symmetric. Spanwise velocity disturbances are ant-symmetric for varicose mode and symmetric for sinuous mode. Taking advantage of the symmetric conditions, the resulting discretized system can be reduced by approximately half. The eigenvalue problem is solved by the QR method which yields all the eigenvalues of the discretized system.

2.2 Direct Numerical Simulation

Linear and nonlinear growth of Görtler vortices at hypersonic speed is numerically simulated using a fifth order upwind shock fitting scheme. Governing equations and numerical schemes are briefly summarized here.

In the numerical simulation, the three-dimensional Navier-Stokes equations (1) to (4) are written in conservative-law form as follows:

$$\frac{\partial U^*}{\partial t^*} + \frac{\partial F^*_j}{\partial x_j^*} + \frac{\partial F^*_{vj}}{\partial x_j^*} = 0 \tag{11}$$

where superscript '$*$' represents dimensional variables and

$$U^* = \{\rho^*, \rho^* u_1^*, \rho^* u_2^*, \rho^* u_3^*, e^*\} \tag{12}$$

$$e^* = \rho^*(C_v^* T^* + \frac{1}{2}u_k^* u_k^*) \tag{13}$$

The flux vectors are

$$F^*_j = \begin{Bmatrix} \rho^* u_j^* \\ \rho^* u_1^* u_j^* + p^* \delta_{1j} \\ \rho^* u_2^* u_j^* + p^* \delta_{2j} \\ \rho^* u_3^* u_j^* + p^* \delta_{3j} \\ (e^* + p^*) u_j^* \end{Bmatrix} \tag{14}$$

$$F^*_{vj} = \begin{Bmatrix} 0 \\ \tau_{1j}^* \\ \tau_{2j}^* \\ \tau_{3j}^* \\ \tau_{jk}^* u_k^* - q_j^* \end{Bmatrix} \tag{15}$$

3

where

$$\tau_{ij}^* = -\mu^* \left(\frac{\partial u_i^*}{\partial x_j^*} + \frac{\partial u_j^*}{\partial x_i^*} \right) + 2\mu^*/3 \frac{\partial u_k^*}{\partial x_k^*} \delta_{ij} \quad (16)$$

$$q_j^* = -\kappa^* \frac{\partial T^*}{\partial x_j^*} \quad (17)$$

μ^* is the viscousity coefficient and calculated using the Sutherland's law:

$$\mu^* = \mu_r^* \left(\frac{T^*}{T_r^*} \right)^{3/2} \frac{T_r^* + T_s^*}{T^* + T_s^*}, \quad (18)$$

and κ^* is the heat conductivity coefficient computed by assuming a constant Prandtl number Pr. The gas is assumed to be thermally and calorically perfect gas,

$$p^* = \rho^* R^* T^* \quad (19)$$

where R^* is the gas constant.

The general curvilinear three-dimensional coordinates (ξ, η, ζ, τ) are used along the body fitted grid lines. A shock fitting method is used to treat the bow shock as a computational boundary. The transformation relations for the current grid systems are

$$\begin{cases} \xi = \xi(x, y, z) \\ \eta = \eta(x, y, z, t) \\ \zeta = \zeta(x, y, z) \\ \tau = t \end{cases} \Longleftrightarrow \begin{cases} x = x(\xi, \eta, \zeta, \tau) \\ y = y(\xi, \eta, \zeta, \tau) \\ y = y(\xi, \eta, \zeta, \tau) \\ t = \tau \end{cases} \quad (20)$$

where $\xi_t = 0$ and $\zeta_t = 0$ because the ξ and ζ grid lines are fixed when the shock boundary moves. In the numerical simulations, the governing equations (11) are transformed into the computational domain (ξ, η, ζ, τ).

$$\frac{1}{J} \frac{\partial U}{\partial \tau} + \frac{\partial E'}{\partial \xi} + \frac{\partial F'}{\partial \eta} + \frac{\partial G'}{\partial \zeta} + \frac{\partial E'_v}{\partial \xi} + \frac{\partial F'_v}{\partial \eta} + \frac{\partial G'_v}{\partial \zeta} + U \frac{\partial(\frac{1}{J})}{\partial \tau} = 0 \quad (21)$$

The governing equation (21) is discretized in the computational domain (ξ, η, ζ, τ). High order finite difference methods are used for spatial discretization of the equation. Inviscid and viscous flux terms are discretized using different methods: fifth order upwind explicit schemes for the inviscid flux terms and central difference schemes for the viscous terms. The time advancement of the governing equations is solved by Runge-Kutta schemes. The shock fitting method treats the bow shock as a computational boundary at $\eta = \eta_{max}$. The flow variables behind the shock are determined by the Rankine-Hugoniot relation across the shock and a characteristic compatibility equation from behind the shock.

3 Results

Linear [16] and nonlinear [17] developments of Görtler vortices in hypersonic boundary layers had been studied by DNS of the full Navier-Stokes equations. The specific test case is a Mach 15 flow over a blunt wedge with a concave surface. The flow conditions in free stream are

$$\begin{aligned} T_\infty^* &= 101.059 K \\ P_\infty^* &= 10.3 Pa \\ T_w^* &= 1000 K \\ Re_\infty &= \rho_\infty^* U_\infty^* / \mu_\infty^* = 150753.175/m \end{aligned} \quad (22)$$

The body surface is assumed to be a non-slip wall with an isothermal wall temperature T_w^*. Two-dimensional steady base flow along the blunt body with concave surface had been first obtained by two-dimensional simulation [16]. Three-dimensional simulation had been carried out for Görlter vortices [16,17]. Figure 1 shows the distributions of Mach numbers and Görtler numbers along the streamwise direction in concave wall region. Mach number and Görtler number ranges in concave surface are from 6 to 9 and from 4 to 14.7 respectively. For the current test case, the Görlter number increases as x increases. For the LST analysis, the Görtler mode is unstable when G is larger than 6. The Görlter modes obtained from the LST code using the simulated two-dimensional base flow were imposed at $G = 6.8$. The subsequent linear and nonlinear developments of the spatially growing longitudinal vortices were solved by computing the full Navier-Stokes equations. Figure 2 shows a schematic of the computational domain.

Nonlinear development of hypersonic Görtler vortices are first presented in this paper which shows the highly inflectional profiles. Since nonlinear Görtler vortices lead to inflection points, we study secondary Görtler instability in hypersonic boundary layers using both 2-D linear stability analysis and numerical simulations. The results of secondary hypersonic Görtler instability are also presented.

4

3.1 Nonlinear Growth of Görtler Vortices

The nonlinear development of Görtler vortices leads to a highly distorted mean flow with inflectional profiles in the wall normal direction as well as the spanwise direction which induce the secondary instabilities of the nonlinear interactions between the Görtler mode and the shear mode. The nonlinear development of Görtler vortices is investigated by imposing the strong disturbances at the entrance of the computational domain. Disturbance amplitude is in the order of $0.2U_\infty$. Imposed disturbances propagate spatially and reach steady state conditions. The strong disturbances distort the two-dimensional base flow and produce the mushroom-shaped vortices and inflectional flow fields in boundary layers. The mushroom-shaped vortices develop due to the counter-rotating vortices pumping action in which low velocity flow moves away from the the wall and the high velocity flow toward the wall. Görtler number of the whole computational domain of the three-dimensional simulation is from 6.8 to 14.7. The corresponding local Reynolds numbers are the range of 4.23×10^5 to 1.33×10^6. Four computational zones are used in nonlinear development of Görtler vortices. The total grid size of the domain is $644 \times 121 \times 64$. Grid independent studies on the nonlinear development of Görtler vortices are used to ensure the numerical accuracy of the results.

Figure 3 shows the streamwise mean velocity (two-dimensional base flow + the primary Görtler mode) distributions as flow moves downstream. The strong vorticity effects distort the two-dimensional base flow. The development of the mushroom-shaped vortices is well represented in the figure which is similar to the incompressible Görtler instability. The figure shows that bow shock does not have much effects on flow field because the shock is far away from the vortices. Figure 4 shows the streamwise mean velocity contours at four different streamwise locations. The region in the neighborhood of the centerline of the vortices is referred to as the peak region, and the region in the side of the vortices is referred to as the valley region. While a displacement thickness in the peak region increases, the one in the valley region decreases downstream. Görtler vortices pump vertically the low-speed fluid away from the wall in the peak region and push the high speed fluid toward the wall in the valley region. As the flow moves downstream, high velocity flow near the surface in the valley region is transferred to the peak horizontally. Such transfer actions of the flow produce the mushroom-shaped vortices. Development of the mushroom-shaped vorticities is illustrated in figure 4. Contours at $x = 1.042$ show the linear development of the disturbances because the shape is

like a cosine curve which is the function of the streamwise velocity perturbations. But it is quickly modified downstream as the Görtler mode disturbances become nonlinear. Figure 5 shows cross sectional velocity vector plots at four different streamwise locations. The counter-rotating vortices are illustrated in the figure. At early station ($x = 1.042$), the vorticity effects are small, but those increase downstream as the disturbances become nonlinear. Flow transfer phenomena in the peak and valley regions is clearly represented in the cross sectional vector. Directions of the vector near the centerline is upward, but the downward for the side regions.

Figure 6 shows the wall normal distributions of the streamwise mean velocity at four different streamwise locations. Each figure contains four curves which represent the four different spanwise locations. The profiles at $K = 4$ and $K = 28$ are for the side and the centerline of the vortices respectively. In the peak region, the pumping action of the counter-rotating vortices gradually generates an S-shaped profile with two inflection points. All wall normal distributions inside the mushroom show the development of the inflection points. The profile at $K = 4$, which is outside of the mushroom, dose not shows the inflection points downstream. As we discussed earlier, as the disturbances become nonlinear, the high speed fluid in the valley near the wall is horizontally transferred to the peak. In figure 6, while the maximum velocity near the surface at $K = 4$ decreases downstream, those inside the mushroom increases which produce a inflection point near the surface. It is an indication of the horizontal flow transfer. The horizontal transfer of the flow is more clearly shown in the streamwise velocity disturbance distributions. Figure 7 shows the streamwise velocity disturbance contours at different streamwise locations. Dashed lines represent negative values of the disturbances. High velocity disturbances in the valley region near the surface move horizontally to the peak region as x increases. On the contrary, the low velocity in the peak region away from the wall moves to the valley. It is due to the action of the counter-rotating vortices. Two inflection points appear in the mushroom near and away from the surface. Figure 8 shows the spanwise distributions of the streamwise mean velocity at four different streamwise locations. The velocity is wake-like profile with inflection points. At $x = 2.754$, the third curve from the bottom shows three minima which is due to the horizontal transfer of the low velocity flow from the peak region to the valley by the counter-rotating vorticity effects. The transfer of low velocity flow causes the side minima in spanwise distribution of the velocity field.

For the numerical accuracy and grid independence of

5

the DNS results, we conduct grid refinment studies on the three-dimensional nonlinear Görtler vortices. The grid size of each computational zone in this paper is 161×121×64. We compute the same case for the fine 321×241×64 grids. The Fourier collocation with 64 grid points in the spanwise direction well resolve the nonlinear Görtler vortices so we keep 64 collocation points in the grid refinment studies. We also compute two Görtler vortices by extending spanwise distance. The grid size is 161×121×128. Each vortex is resolved by 64 spanwise grids points. Figure 9 shows the comparison of the results from two different sets of grids at $x = 1.34$. The comparison shows the grid independence in streamwise and wall normal directions. The figure also shows that the vortices dose not interact with other neighboring vortices in the spanwise direction which represents that the simulation of one Görtler vortex is enough in order to study the nonlinear Görtler instabilities.

3.2 Secondary Instability of Hypersonic Görtler Vortices

We showed that the nonlinear development of Görtler vortices produce inflection points not only in wall normal direction but also in spanwise direction which is similar to incompressible flow. These inflection points are associated with the secondary instability of the nonlinear interaction between the Görtler mode and the shear mode. Such secondary instability may be responsible for the nonlinear break-down and transition to turbulence in the Görtler instability. We study secondary instability of hypersonic Görtler vortices using two-dimensional linear stability analysis and numerical simulation. We develop a two-dimensional LST code for secondary instability because the secondary modes are two dimensional. The secondary mode obtained by a two-dimensional LST code is imposed at the entrance of the computational domain. Subsequent development of the secondary mode is carried out by solving the full Navier-Stokes equations.

A two-dimensional LST analysis is applied to the distorted mean flow obtained in the nonlinear DNS study of Görtler vortices in Mach 15 flow over a blunt wedge. There are two kinds of secondary instability modes: sinuous and varicose. We find such modes using the nonlinear simulated results. We search the modes in a range of ω at $x = 1.7$ and $G = 10.3$. At this location, the mushroom-shaped vortices are not fully developed, but the nonlinear effects of Görtler vortices are significant. In the two-dimensional LST analysis, we consider the spatial secondary instability. A wave frequency ω is given, and streamwise wavenumber α

and corresponding eigenfunctions are computed in an eigenvalue calculation. At $x = 1.7$, we find the first varicose and sinuous modes, but those are stable. Figure 10 shows the eigenfunction contours for the first varicose mode at $\omega = 80.0$. A growth rate α_i of this mode is 0.8. Positive α_i represents the mode is stable. The eigenfunctions in figure 10 shows the symmetric or anti-symmetric characteristics of the varicose mode. All eigenfunctions except spanwise velocity disturbance are symmetric in the spanwise direction, but spanwise velocity components are anti-symmetric. In the incompressible Görtler instability, it had been shown that the varicose mode is associated with the wall normal gradients of streamwise mean velocity and the sinuous mode is with the spanwise gradients. [7,12–14] We compare the structures of the wall normal streamwise mean velocity gradient obtained from the nonlinear DNS study with those of the varicose mode from the two-dimensional LST analysis. Figure 11 shows the contours of the wall normal gradients and a root mean square of streamwise velocity eigenfunctions. The figure shows that the location of the peak in the low velocity region away from the surface is the same in both contours. The varicose mode is related to the vertical shear and caused by inflection points in the wall normal direction.

We also find the sinuous mode at the same location for the same wave frequency ω. The growth rate of the mode obtained from the LST analysis at $\omega = 80.0$ is 3.9. The positive growth rate represents the mode is stable. The growth rate of the sinuous mode is larger than the one of the varicose. It shows that the sinuous mode is more stable than the varicose mode at $x = 1.7$. In other words, the varicose mode is the dominate instability over the sinuous mode at this location. Figure 12 shows the contours of the eigenfunctions of the first sinuous mode. The sinuous mode has an anti-symmetric structure in all disturbances except the spanwise velocity component. It is well represented in the figure. Streamwise velocity, pressure, and temperature eigenfunctions are ant-symmetric in the spanwise direction, but the spanwise velocity component is symmetric. The sinuous mode is associated with the spanwise gradients of the streamwise mean velocity obtained by a nonlinear DNS study of Görtler vortices. Figure 13 compares the spanwise gradients of the DNS results with a root mean square of streamwise velocity eigenfunctions of the two-dimensional LST results. The comparison shows that the peaks of the eigenfunction appear at the peaks of the velocity gradient. It represents that the sinuous mode is associated with the inflection points in the spanwise direction.

The two-dimensional LST analysis shows that the varicose mode is the dominate instability over the sin-

6

uous mode at $x = 1.7$. The two-dimensional LST analysis is conducted for the whole computational domain, and growth rate α_i is compared with respect to x. Figure 14 shows a such comparison. The figure represents that the mode is stable in whole computational domain since α_i is positive for all x. However, the magnitude become less positive as x increases which represents the mode are more unstable as flow moves downstream.

We conduct a DNS study of the secondary instability of Görtler vortices by imposing the varicose mode at the entrance of the computational domain located at $x = 1.7$. A range of Görtler number in the domain is 10.2 to 12.9. A local Reynolds number is between 7.80×10^5 and 1.10×10^6. Amplitudes of the imposed secondary disturbances are 0.1% of the freestream velocity. The disturbances propagate spatially in the streamwise direction and reach a periodic condition. Figure 15 shows the contours for streamwise velocity disturbances obtained by the DNS of secondary instability for Mach 15 flow over a blunt body with concave surface. The disturbances develop into a mushroom like structure which is characteristic of the varicose mode. Figure 16 is the instantaneous cross sectional contours in the wall normal direction. Although the mode is stable at the inlet, the figure also shows that some cross sections show growing disturbance by the intensity in the middle of the section.

Fourier analysis is carried out on the numerical solution of secondary Görtler instability. Fourier transform of a disturbance variable is expressed to:

$$q'(x, y, z, t) = \sum_{m=0}^{M} \sum_{n=0}^{N} q'_{mn}(x, y) e^{i[m\omega t + n\beta z + \phi_{mn}]} \quad (23)$$

where β and ω is the spanwise wave number and frequency of inlet disturbance, and $q'(x, y, z, t)$ represents any perturbation variables. $q'_{mn}(x, y)$ and ϕ_{mn} are the local perturbation amplitudes and phase angles. The integer m and n represent the wave mode of the perturbation fields. In our numerical results, a dominant wave mode is $(m, n) = (1, 1)$. Since the imposed disturbances are weak, magnitudes of other modes are small. Figure 17 shows the magnitude of streamwise velocity disturbance amplitude ($|u_{11}|$) as a function of x. The magnitude is defined as

$$|u_{11}| = \sqrt{u_r^2 + u_i^2} \quad (24)$$

where u_r and u_i represent real and imaginary parts of the local perturbation amplitude. The figure shows the streamwise distributions of magnitudes for several

different wall normal locations. Perturbation amplitude near the surface initially increases but starts to decrease at later station. However, disturbance amplitude away from the surface increases. For example, the amplitude at $y = 0.003$ starts to decrease at $x \approx 1.9$, but the one at $y = 0.028$ increases in the whole x ranges. Nonlinear development of Görtler vortices produce inflection points between $y = 0.01$ and $y = 0.05$ (figure 6). Such inflection points cause increase disturbances.

We do some preliminary comparison on the wave structure between DNS results and those obtained from 2-D secondary instability analysis. Figure 18 compares eigenfunctions from DNS with those obtained from two-dimensional LST analysis at $x = 2.0$. The wave structures of streamwise velocity, temperature and spanwise velocity components from both DNS and LST are shown in the figure. The two sets of results are similar.

Having studied linear development of varicose mode by imposing weak disturbances at the entrance of computational domain, we impose strong disturbance at the same location and conduct the nonlinear development of the mode. The amplitude of the inlet disturbances is in the order of 5% of freestream velocity. We observe that the strong disturbances distort steady Görtler vortices. Figure 19 shows the instantaneous streamwise velocity contours in the (x, z) plane at various wall normal locations. Left figures represents the contours of steady Görtler vortices without varicose mode, and those on the right are the contours with varicose mode. Large amplitude varicose mode change Görtler vortices into series of knotty structure associated with the horseshoe vortex mode of break down. Streamwise velocity contours in the (x, y) plane also shows the distortion of steady Görtler vortices. Figure 20 represents the contours at various spanwise locations. Left figures are the contours without varicose mode, and the rights are those with varicose mode. The figure shows that varicose mode imposed at the entrance of computational domain propagates spatially and changes Görtler vortices into wave motion.

2-D LST analysis shows anti-symmetric characteristic of spanwise velocity perturbation and the symmetric of other variables of varicose mode. Therefore, we examine the structures of spanwise mean velocity for both with and without varicose mode. Figure 21 shows the instantaneous spanwise mean velocity contours at various wall normal locations. Although the spanwise velocity has anti-symmetric structure in spanwise direction, varicose mode spatially propagates in the manner of horseshoe vortex motion. The contours near the surface such as $y = 0.0007$ and $y = 0.003$

7

show the knotty structure in the middle portion of the figures. Such structure is also observed in the contours away from the surface such as $y = 0.036$ and $y = 0.063$. However, for these cases, horseshoe vortex motion appears both sides of a center line. Figure 22 shows the spanwise mean velocity contours in the (x, y) plane at various spanwise location. As the case of streamwise velocity discussed earlier, varicose mode distort the spanwise velocity of Görtler vortices into wave motion. Other flow variables show the similar structure of streamwise mean velocity, so those are not presented in this paper. From the numerical solutions of nonlinear interactions between varicose mode and Görtler vortices, we can conlude that varicose mode distort Görtler vortices and may break down the vortices into turbulence.

4   Summary

Nonlinear development of Görtler vortices and secondary instability effects in hypersonic boundary layers have been studied by 2-D linear stability analysis and numerical simulations. In the nonlinear development of Görtler vortices, the counter rotating vorticity effects transferred the low velocity flow away from the surface and high velocity flow toward the surface. Such effects lead to the mushroom-shaped vortices with inflection points in both wall normal and spanwise directions which induce secondary instability effects. In order to study secondary Görtler instability, we developed 2-D LST code and found the secondary modes. In 2-D LST analysis, both sinuous and varicose modes were found. We imposed varicose mode at the entrance of computational domain since the LST analysis showed varicose mode was more unstable than sinuous mode for our flow conditions. For linear development of varicose mode, weak disturbances were introduced on steady Görtler vortices. Simulation results were compared with those obtained from 2-D LST analysis. Such comparison showed a good agreement. By imposing large amplitude of varicose mode, we studied nonlinear interaction between varicose mode and Görtler vortices. The numerical results showed that the strong varicose mode breaks down Görtler vortices into horseshoe vortex.

5   Acknowledgments

References

[1] Görtler, H., "Instabilita-umt laminarer Grenzchichten an Konkaven Wäden gegenber gewissen dreidimensionalen Störungen," *ZAMM*, Vol. 21, 1941, pp. 250-52.

[2] Aihara, Y., "Görtler vortices in the nonlinear region," In Theoretical and Experimental Fluid Mechanics, ed U. Müller, K. G. Roesner, B. Schmidt, pp 331-38. Berlin:Springer-Verlag, 1979.

[3] Winoto, S. H. and Crane, R. I., "Vortex structure in laminar boundary layers on a concave wall," *Intl. J. Heat Fluid Flow*, Vol. 2, 1980, pp. 221-231.

[4] Peerhossaini, H. and Wesfreid, J. E., "Experimental study of the Taylor-Görtler Instability," In Propagation in Systems Far From Equilibrium, ed. J. E. Wesfreid, H.R. Brand, D. Manneville, G. Albinet, N. Boccara, et al, pp. 399-412. Berlin:Springer-Verlag, 1988.

[5] Aihara, Y. and Koyama, H., "Nonlinear development and secondary instability of Görtler Vortice," In Stability in the Mechanics on Continua, ed F. H. Schroeder, pp 345-54. Berlin: Springer-Verlag, 1982.

[6] Y. Aihara, Y. T. and Ito, A., "Generation, development and distortion of longitudinal vortices in boundary layers along concave and flat plates," In Laminar-Turbulent Transition, ed V. V. Kozlov, pp. 447-54. New York:Springer-Verlag, 1985.

[7] Swearingen, J. D. and Blackwelder, R. F., "The growth and breakdown of streamwise vortices in the presence of a wall," *J. Fluid Mech.*, Vol. 182, 1987, pp. 255-290.

[8] Hall, P., "The nonlinear development of Görtler vortices in growing boundary layers," *J. Fluid Mech.*, Vol. 193, 1988, pp. 243-266.

[9] Denier, J. P. and Hall, P., "On the nonlinear development of the most unstable Görlter vortex mode," *J. Fluid Mech.*, Vol. 231, 1991, pp. 615-663.

[10] Sabry, A. S. and Liu, T. C., "Longitudinal vorticity elements in boundary layers: nonlinear development from initial Görlter vortices," *J. Fluid Mech.*, Vol. 231, 1991, pp. 615-663.

[11] Lee, K. and Liu, T. C., "On the growth of mush-roomlike structure in nonlinear spatially developing Görtler vortex flow," *Phys. Fluids A*, Vol. 4(1), 1992, pp. 95–103.

[12] Liu, W. and Domaradzki, J. A., "Direct numerical simulation of transition to turbulence in Görtler flow," *J. Fluid Mech.*, Vol. 246, 1993, pp. 267–299.

[13] Yu, X. and Liu, T. C., "On the mechanism of sinous and varicose modes in three-dimensional viscous secondary instability of nonlinear Görtler rolls," *Phys. Fluids*, Vol. 6(2), 1994, pp. 736–50.

[14] Li, F. and Malik, M., "Fundamental and subharmonic secondary instabilities of Görtler vortic es," *J. Fluid Mech.*, Vol. 297, 1995, pp. 77–100.

[15] Ito, A., "Breakdown structure of longitudinal vortices along a concave wall," *J. Japan Soc. Aerospace Sci.*, Vol. 33, 1985, pp. 166–173.

[16] Whang, C. and Zhong, X., "Direct numerical simulation of Görlter instability in hypersonic boundary layers," *AIAA Paper 99-0291*, 1999.

[17] Whang, C. and Zhong, X., "Nonlinear interaction of Görtler and second shear modes in hypersonic boundary layers," *AIAA Paper 2000-0536*, 2000.
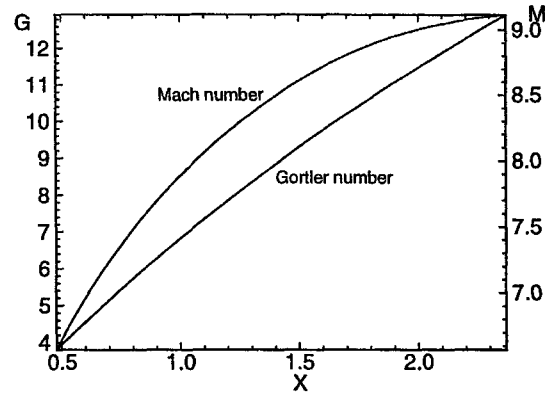
Figure 1: Distributions of Görtler number and Mach number behind shock. Görtler number increases since Reynold's number increases.
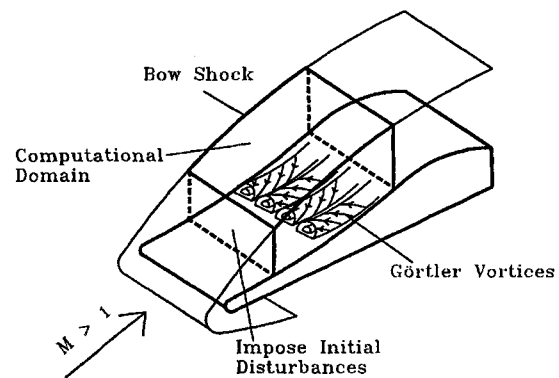
Figure 2: A schematic of computational domain of two-dimensional base flow and three-dimensional Görtler instability simulation.

9
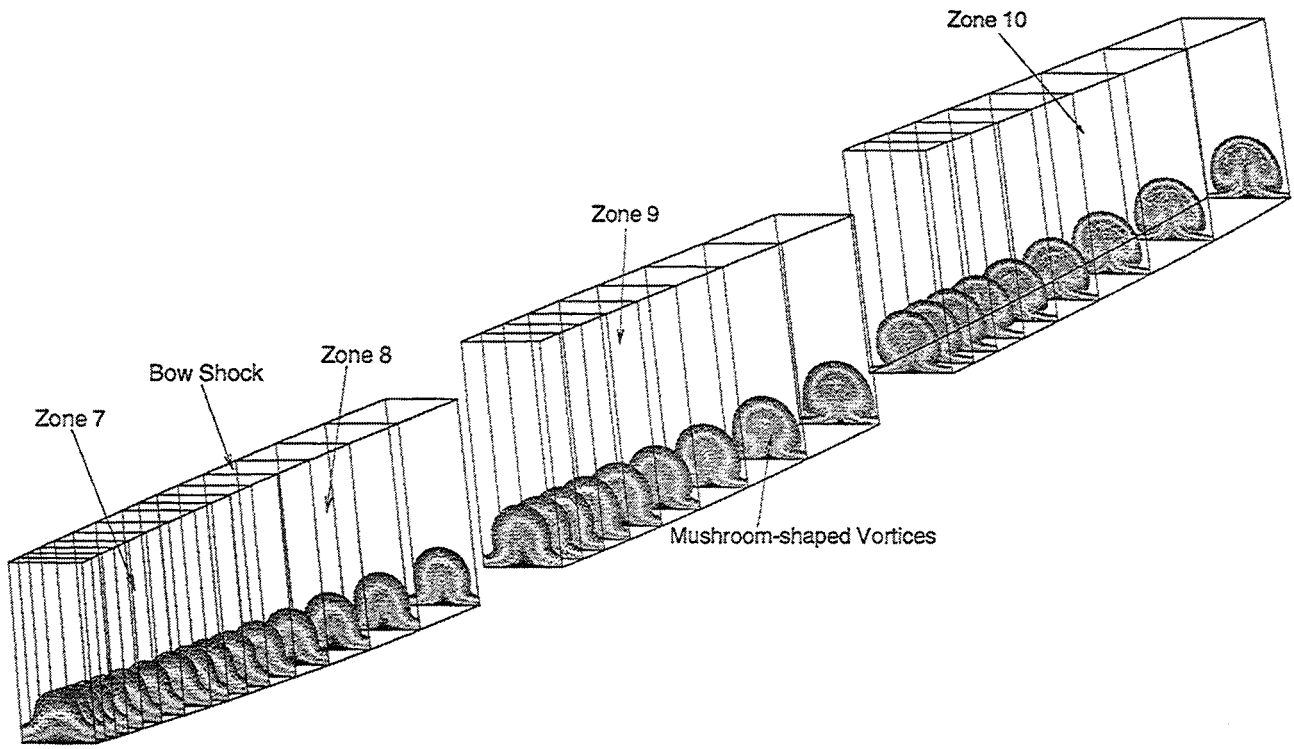
Figure 3: Distributions of streamwise mean velocity contours along the streamwise direction. Mushroom-shaped vortices develop as flow moves downstream due to the nonlinear effects.
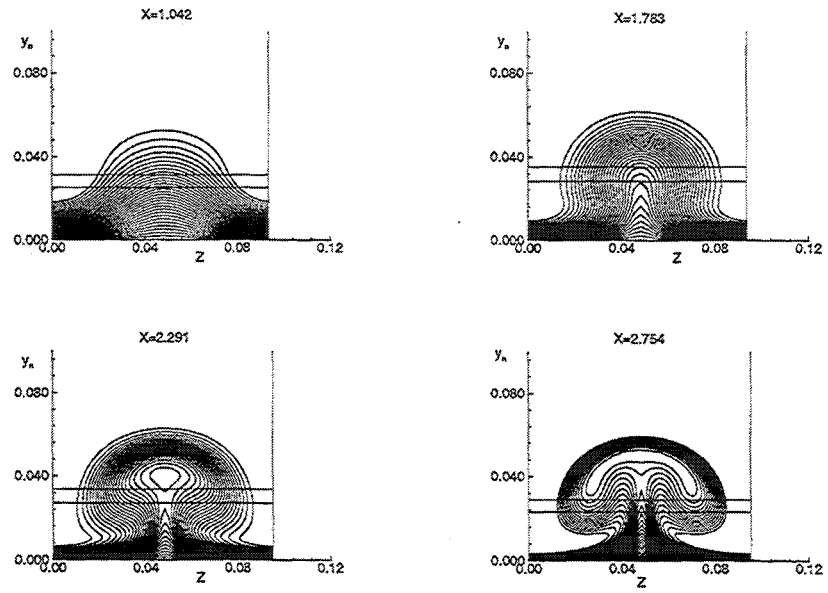
Figure 4: Sectional streamwise mean velocity distributions at four different streamwise locations.

10
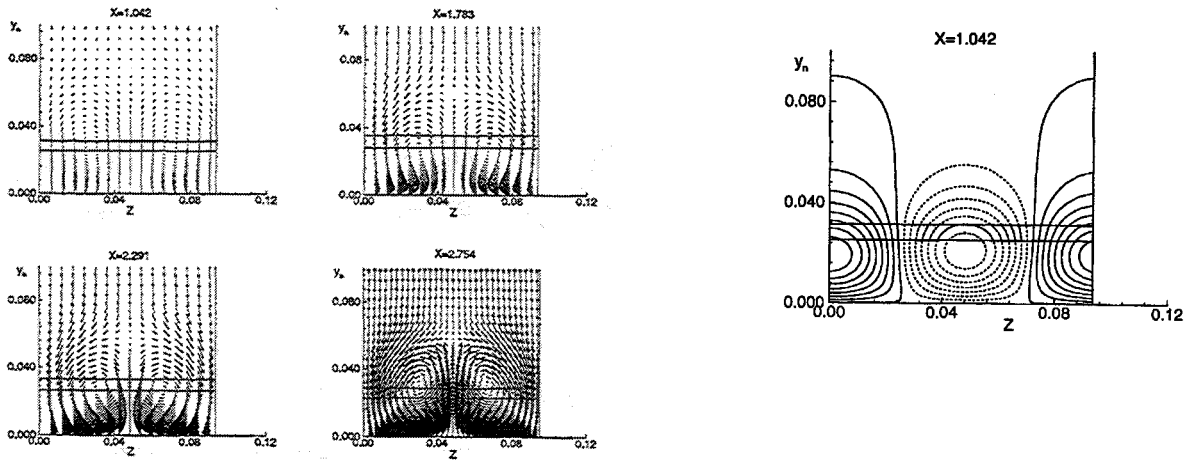
Figure 5: Structure of the velocity vector field in the plane normal to the wall.
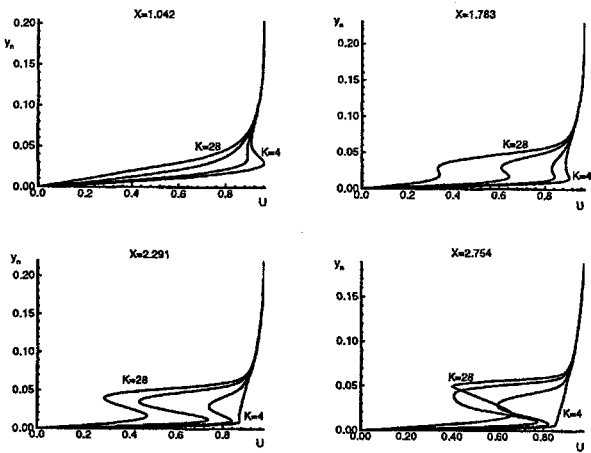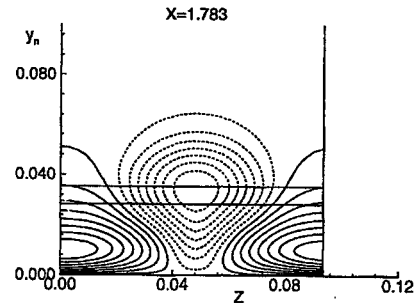
Figure 6: Profiles of the streamwise velocity in wall normal direction at four different streamwise locations. Two inflection points develop in the region of the mushroom.
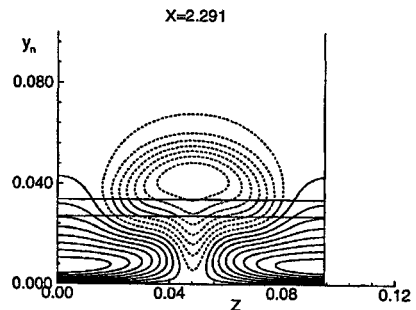
Figure 7: Streamwise velocity disturbance contours at four different streamwise locations. Disturbances in valley region near the wall moves to the peak region of Görtler vortices.
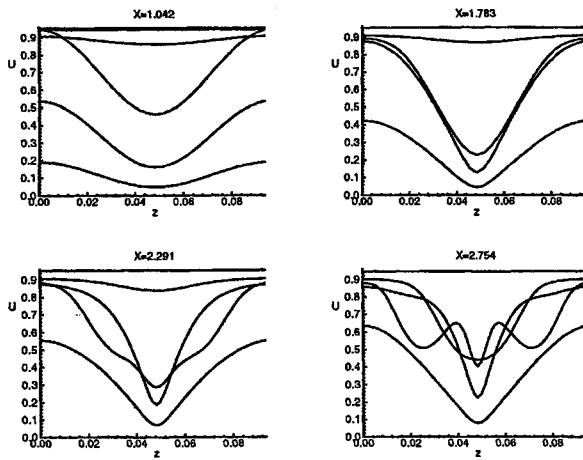
Figure 8: Profiles of the streamwise mean velocity in spanwise direction at four different streamwise locations.
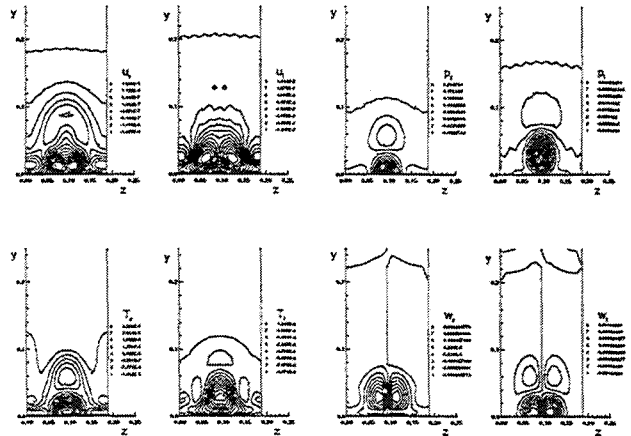
Figure 10: Eigenfunctions for the varicose mode at $x = 1.7$, $G = 10.3$ and $\omega = 80.0$.
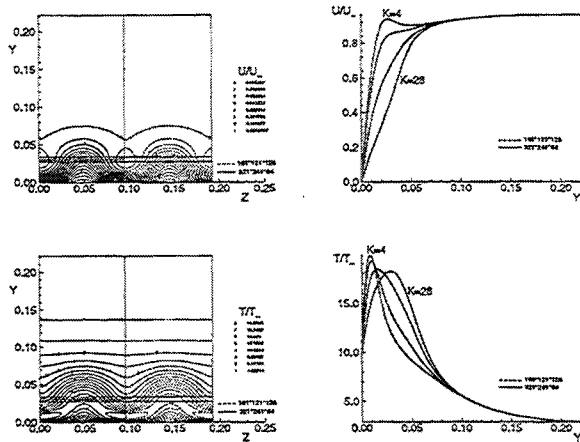
Figure 9: Comparisons of double grids with one Görtler vortex and single grids with two Görtler vortices at the end of the computational domain.
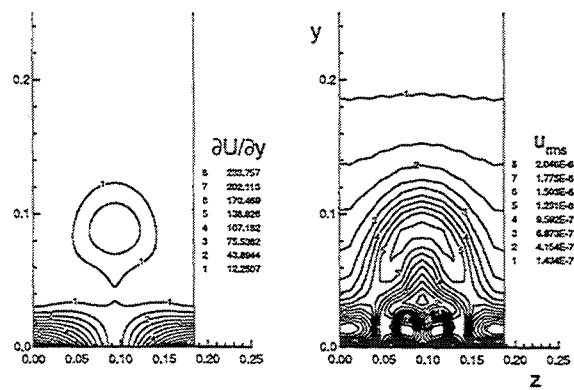
Figure 11: Comparison of the wall normal gradients of streamwise mean velocity and a root mean square of streamwise velocity eigenfunction of the sinuous mode.

12
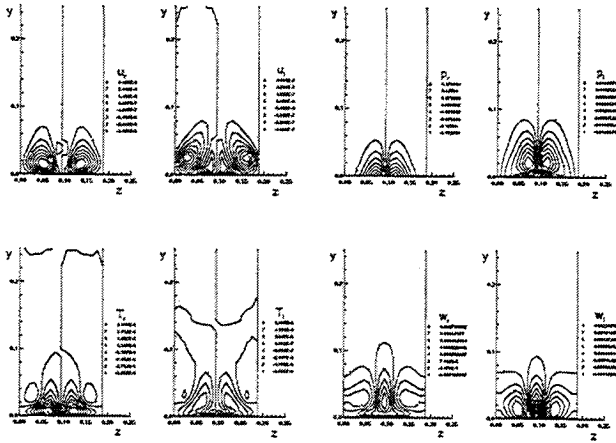
Figure 12: Eigenfunctions for the sinuous mode at $x =$ 1.7, $G = 10.3$ and $\omega = 80.0$.
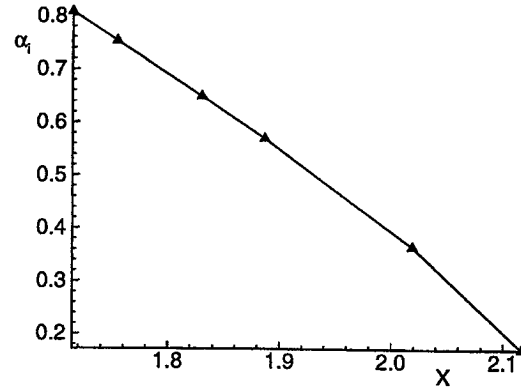
Figure 14: Growth rate (α_i) comparison of varicose mode with respect to x at $\omega = 80$
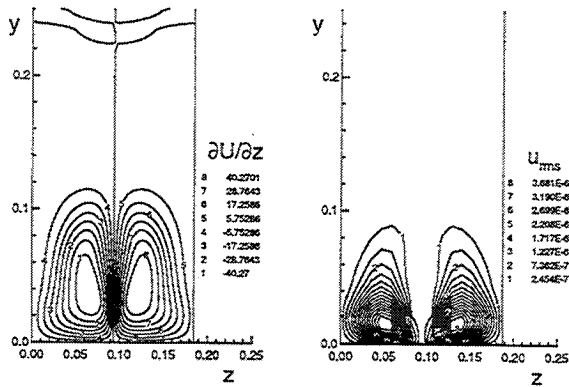
Figure 13: Comparison of the spanwise gradients of streamwise mean velocity and a root mean square of streamwise velocity eigenfunction of the sinuous mode.
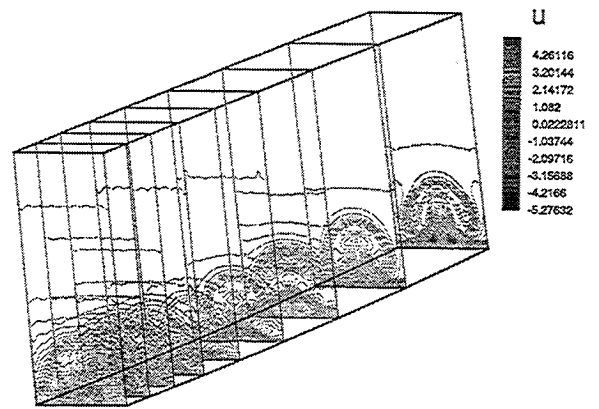
Figure 15: Cross sectional contours for streamwise velocity disturbances of the varicose mode in streamwise direction with $\omega = 80.0$ at inlet of the computational domain.
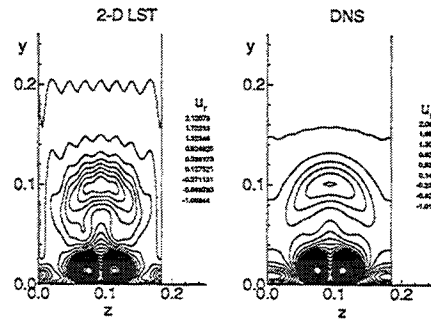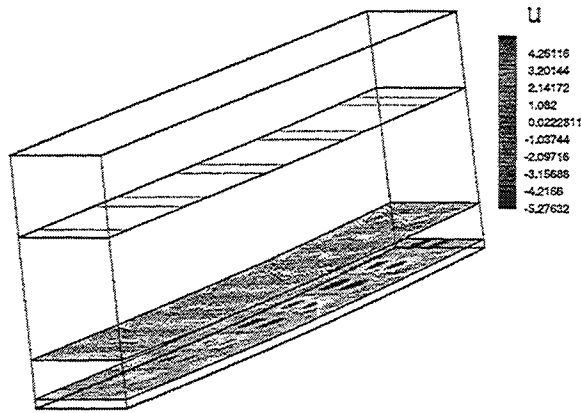
Figure 16: Cross sectional contours for streamwise velocity disturbances of the varicose mode in wall normal direction with $\omega = 80.0$ at inlet of the computational domain.
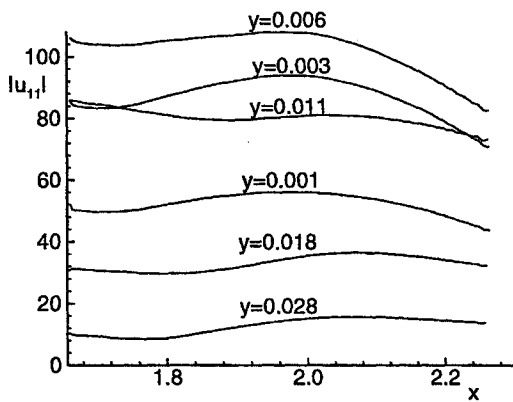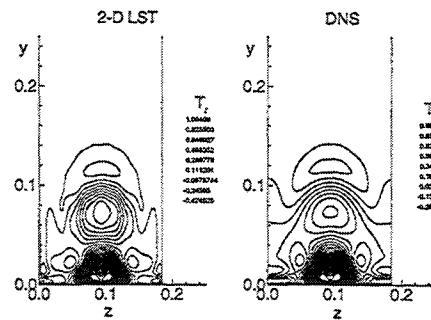
Figure 17: Magnitude of streamwise velocity disturbance amplitude of (1,1) mode as a function of x obtained by Fourier analysis.
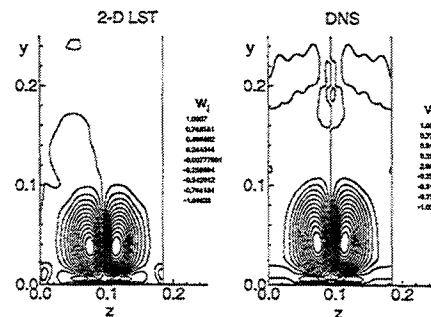
Figure 18: Comparison of the wave structure between DNS results and those obtained from 2-D secondary instability analysis at $x = 2.0$

14

(a) y=0.0007

(a) z=0.01

(b) y=0.003

(b) z=0.02

(c) y=0.036

(c) z=0.05

(d) y=0.063

Without varicose mode   With varicose mode
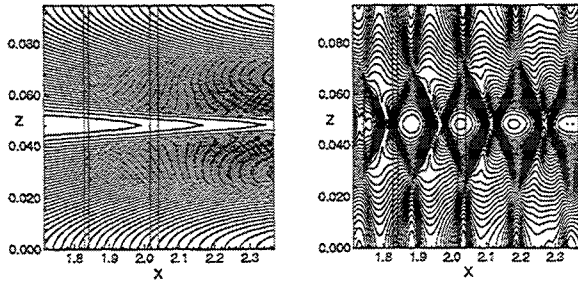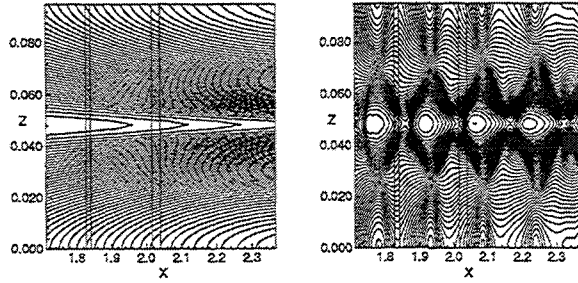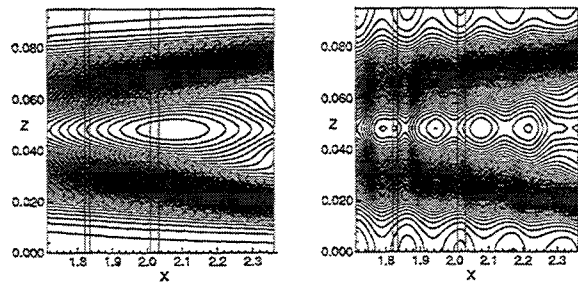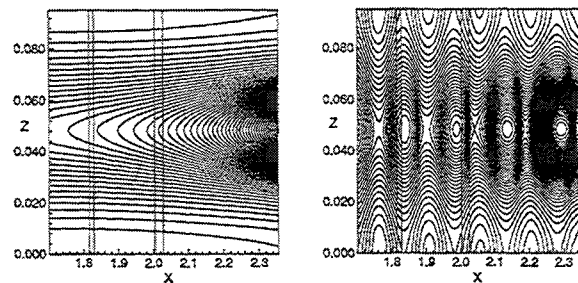
Without varicose mode   With varicose mode

Figure 19: Cross sectional contours of streamwise velocity at various wall normal locations. Left figures represent streamwise velocity contours without varicose mode, and right figures are the contours with varicose mode
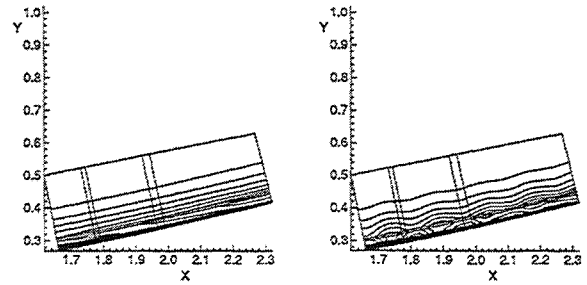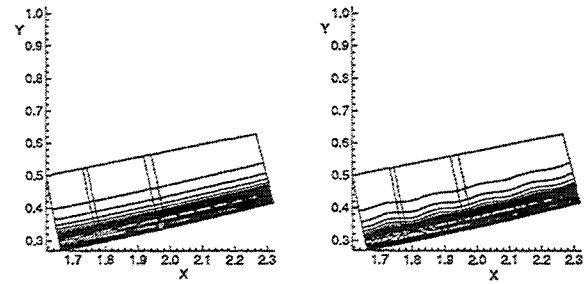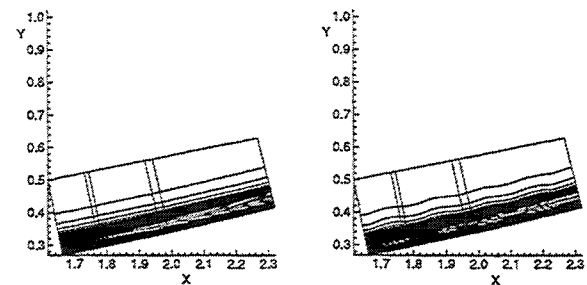
Figure 20: Cross sectional contours of streamwise velocity at various spanwise locations. Left figures represent streamwise velocity contours without varicose mode, and right figures are the contours with varicose mode

15

(a) y=0.0007

(a) z=0.01

(b) y=0.003

(b) z=0.02

(c) y=0.036

(c) z=0.05

(d) y=0.063

Without varicose mode   With varicose mode
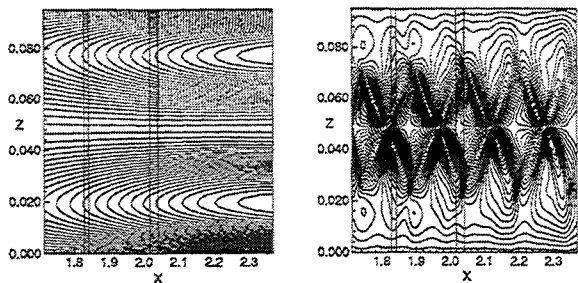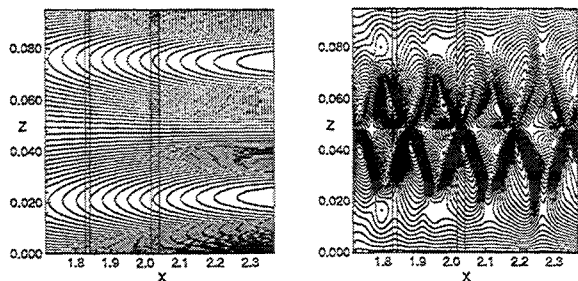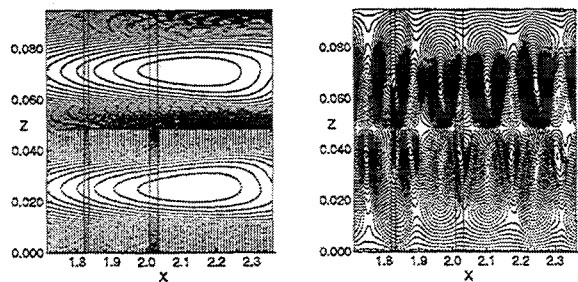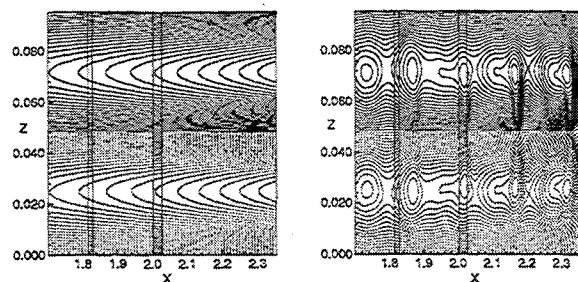
Without varicose mode   With varicose mode

Figure 21: Cross sectional contours of spanwise velocity for four different wall normal locations.
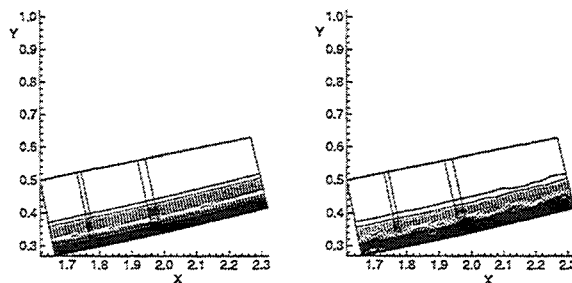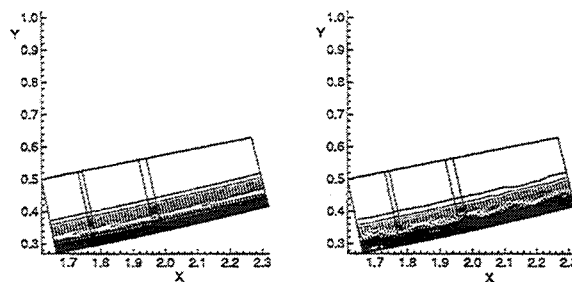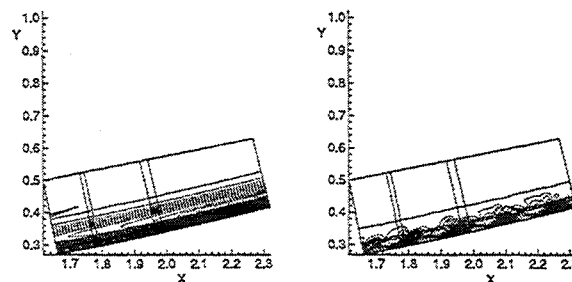
Figure 22: Cross sectional contours of spanwise velocity at various spanwise locations.

16